Buried Interface Passivation of Perovskite Solar Cells by ALD Al$_2$O$_3$

Sudeshna Ghosh,[1] Debasmita Pariari,[2] Tejmani Behera,[3] Pablo P. Boix,[4] Narasimha Ganesh,[5] Susmita Basak,[6] Arya Vidhan,[6] Nisha Sarda,[6] Iván Mora-Seró,[7] Arindam Chowdhury,[3] Kavassery Sureswaran Narayan,[5] D. D. Sarma,[2*] and Shaibal K. Sarkar [6*]

1 Center for Research in Nanotechnology and Science, Indian Institute of Technology Bombay, Powai 400 076 Mumbai, India.

2 Solid State and Structural Chemistry Unit, Indian Institute of Science, Bengaluru – 560012. India

3 Department of Chemistry, Indian Institute of Technology Bombay, Powai 400 076 Mumbai, India.

4 Institut de Ciència dels Materials, University of Valencia Catedràtic J. Beltran 246980 Paterna, Valencia, Spain.

5 Chemistry and Physics of Material Unit (CPMU), Jawaharlal Nehru Center for Advanced Scientific Research, Bengaluru 560064, India.

6 Department of Energy Science and Engineering, Indian Institute of Technology Bombay, Powai 400 076 Mumbai, India.

7 Institute of Advanced Materials, Universitat Jaume I, Av. de Vicent Sos Baynat, s/n

12071Castelló de la Plana, Spain.

Corresponding Author

*sarma@iisc.ac.in

*shaibal.sarkar@iitb.ac.in

Experimental section

FTO substrate preparation: F: SnO_2 (FTO, Tech-8) sheets were purchased from Dyesol. Zn powder (Merck) and 2M HCl (Rankem) acid were used to etch 3X3 cm FTO substrates. The cleaning process of FTO substrates was started with Alconox water solution followed by de-ionized water, acetone, and isopropanol solvents, for 10 min each. After that, the drying process of the FTO substrates was completed followed by 30 minutes of UV treatment.

SnO_2 ETL deposition: A 30 nm bi-layer SnO_2 as ETL was spin-coated on FTO substrates. 0.05M concentration planar SnO_2 solution was prepared by dissolving tin (IV) chloride pentahydrate ($SnCl_4.5H_2O$ - 98%, Sigma Aldrich) in anhydrous isopropanol (99.5 %, Sigma Aldrich). The deposition of SnO_2 solution was done by spin coating process at 2000 rpm for 45 seconds on FTO substrates followed by annealing at 180ºC for 50 minutes. For bi -layer formation, nP- SnO_2 layers were prepared by the spin casting of aqueous Alfa Aesar nanoparticle suspension diluted in DI water (1:4) at 4000 rpm for 45 s followed by annealing in ambient air at 150 ^{0}C for 30 min. Prior to Colloidal SnO_2 deposition, 30 min UV-ozone treatment was applied on the Planar SnO_2 coated FTO substrates.

TiO_2 ETL deposition: For the deposition of TiO_2 compact, dense layer on the cleaned FTO substrate, 3 layers of compact TiO_2 precursor solution were spin-coated at 4000 rpm for 30 sec. (1st two layers were deposited using 0.13 M solution of Titanium di-isopropoxide bis (acetylacetonate) in 1-butanol and 3rd layer was deposited using 0.26 M solution and after spin coating of each layer, the film was dried at 100ºC for 10 min. After 3 layers of spin coating and drying of Compact TiO_2 precursor solution, the film was annealed at 500 ºC for 30 min with a 5 ºC/min ramp in the muffle furnace. After that, TiO_2 mesoporous layer was deposited over the c-

TiO$_2$ layer with 20 min of UV-Ozone cleaning by spin coating of TiO$_2$ paste (30-NRD, Dyesol) diluted in ethanol (1:6 by weight) at 4000 rpm for 30 sec with 2000 rpm/sec followed by drying at 100 ºC for 10 min and annealing at 500 ºC for 30 min with 5 ºC/min ramp in the muffle furnace. Before Mesoporous TiO$_2$ deposition, 20 min UV-ozone treatment was applied on the dense TiO$_2$-coated FTO substrates. For the TiCl$_4$ treatment, 20 mM TiCl$_4$ (Sigma-Aldrich, 98%) solution was prepared in DI water and TiO$_2$-coated substrates were immersed in the solution and then, kept at 100 ºC in the oven for 50 min, followed by annealing in the muffle furnace at 500℃ for 30 min with 5 ºC/min ramp.

((FA $_{0.83}$ MA $_{0.17}$) $_{0.95}$ Cs $_{0.05}$ PbI $_{2.5}$ Br $_{0.5}$ Perovskite absorber fabrication: The preparation of triple cation mixed halide perovskite absorber, ((FA $_{0.83}$ MA $_{0.17}$) $_{0.95}$ Cs $_{0.05}$ PbI $_{2.5}$ Br $_{0.5}$ was made by using 1M formamidine iodide (FAI) (Greatcell Solar Materials) of 1M, methylamine bromide (MABr), (>99.99%, Greatcell Solar Materials) of 0.2M, lead iodide (PbI$_2$),(99.9%, Tokyo Chemical Industries) of 1.1 M, PbBr$_2$ lead bromide (PbBr$_2$), (99.9%, Tokyo Chemical Industries) of 0.2M dissolved in dimethylformamide (DMF), (anhydrous, 99.8%, Sigma Aldrich), dimethyl sulfoxide (DMSO), (anhydrous, 99.9%, Sigma Aldrich) in the volume ratio of 4:1 followed by stirring for 2 hours. Later, 52 µl solution from 1.5 M of a stock solution containing Cesium iodide (CsI), (99.999%, Tokyo Chemical Industries) dissolved in DMSO solvent was mixed with previously prepared precursor solution of volume 1ml followed by stirring. The spin-coating process of perovskite solution was done on SnO$_2$ /TiO$_2$ coated FTO substrates using an anti-solvent assisted spin-coating process of the rpm of 2000 and 6000 rpm for 10sec and 30sec respectively. Prior to perovskite deposition, 30 min UV-ozone treatment was applied on the SnO$_2$/TiO$_2$ coated FTO substrates. Antisolvent of 500 µl of chlorobenzene (anhydrous, 99.8%, Sigma Aldrich) was dripped on spinning substrates 15sec before the end of the 30sec spinning program as solvent

quencher followed by annealing at 100 ºC for 50 minutes inside a glove box containing nitrogen atmosphere.

MAPbI₃ perovskite absorber preparation:1.4 M MAPbI$_3$ solution was prepared by mixing the MAI ((>99.99%) Greatcell Solar Materials) & PbI$_2$ ((99.99%, trace metals basis, TCI chemicals) (1:1 by mole) in DMF (anhydrous, 99.8%, Sigma Aldrich): DMSO (anhydrous, 99.9%, Sigma Aldrich) from (9:1 by vol.) and Stirred at room temperature for 5 hrs. For the process of spin-coating the MAPbI$_3$ solution, 200 µl solution spread over the entire surface of SnO$_2$ ETL coated FTO substrate and spin-coated at 4000 rpm with 1000 rpm/s acceleration for 30 sec. Just after completion of 10 sec. rotation antisolvent of 500 µL chlorobenzene was dripped on the substrate during spinning. Finally, annealed at 85 ºC for 2 min followed by annealed at 100 ºC for 8 min.

OLAI (2D) passivation:0.5 mg Oleylammonium iodide (OLAI), purchased from Xi'an Polymer L.T, dissolved in 1mL anhydrous IPA (99.5 %, Sigma Aldrich) for 2D passivation. The solution was spin-coated onto as prepared perovskite film at 5000 rpm for 25sec in N$_2$ -filled glove box and stored overnight in a dark and N$_2$ environment in the glove box. The devices are washed with IPA at 5000 rpm for 20sec to remove unbounded 2D ligands.

Spiro-OMeTAD HTL preparation: Spiro-OMeTAD of 80 mg (Luminescence Technology) was dissolved in chlorobenzene of 1 ml followed by the addition of 24 µl of 26 mg bis (trifluoromethane) sulfonamide lithium salt (Sigma Aldrich) dissolved in acetonitrile (anhydrous, 99.8%, Sigma Aldrich) and 40 µl of 4-tert-butylpyridine (Sigma Aldrich). Spiro-OMeTAD of 80 µl solution was spin-coated dynamically on as prepared films at 4000 rpm for 45sec followed by oxidation process of spiro-OMeTAD by leaving films overnight under ambient conditions.

Gold Metal Contact: Thermal evaporation of 80 nm gold metal (99.999%, Parekh Industries) is done inside a vacuum chamber with a base pressure 5×10^{-6} mbar to make connections. A shadow mask is used to define the active area of the devices of approximately 0.12 cm^2.

Atomic layer Al$_2$O$_3$ deposition: A thin layer of Aluminium oxide (Al$_2$O$_3$) was deposited on top of devices inside a custom-built viscous flow hot wall rector configuration at 70 °C. Trimethyl aluminum (TMA, from Gelest, Inc) and HPLC grade H$_2$O (from Sigma Aldrich, USA) are used as precursors. [1] Nitrogen (N$_2$, 99.999%), which served as a carrier gas, was used during this deposition. A further discussion of the reactor is given elsewhere. [2] (n-t1-m-t2) was used here as the precursor pulsing arrangement, where 'n' and 'm' are the number of pulses of TMA and H$_2$O while 't1' and 't2' were the purge times after TMA and H$_2$O in seconds respectively where t1 is 10 sec and t2 is 10 sec respectively. The dose times of 1 sec were maintained for both reactants throughout the experiment. The variation of transient pressure ca. 0.1 ± 0.05 Torr and 0.6 ± 0.05 Torr were maintained during the TMA and H$_2$O exposures of 1 sec respectively followed by continuous monitoring with the help of capacitance manometer (MKS). In our case, 300 cycles of the ALD cycles were found optimized for the performance. Under the ideal scenario, each ALD cycle with the above cycle leads to 0.12nm, hence ideally the thickness is likely to be 36nm. But due to, the non-linear nucleation of the Al$_2$O$_3$ on spiro surely leads to a deviation from the standard calculation. Devices were taken immediately out of the ALD reactor upon completion of the reaction.
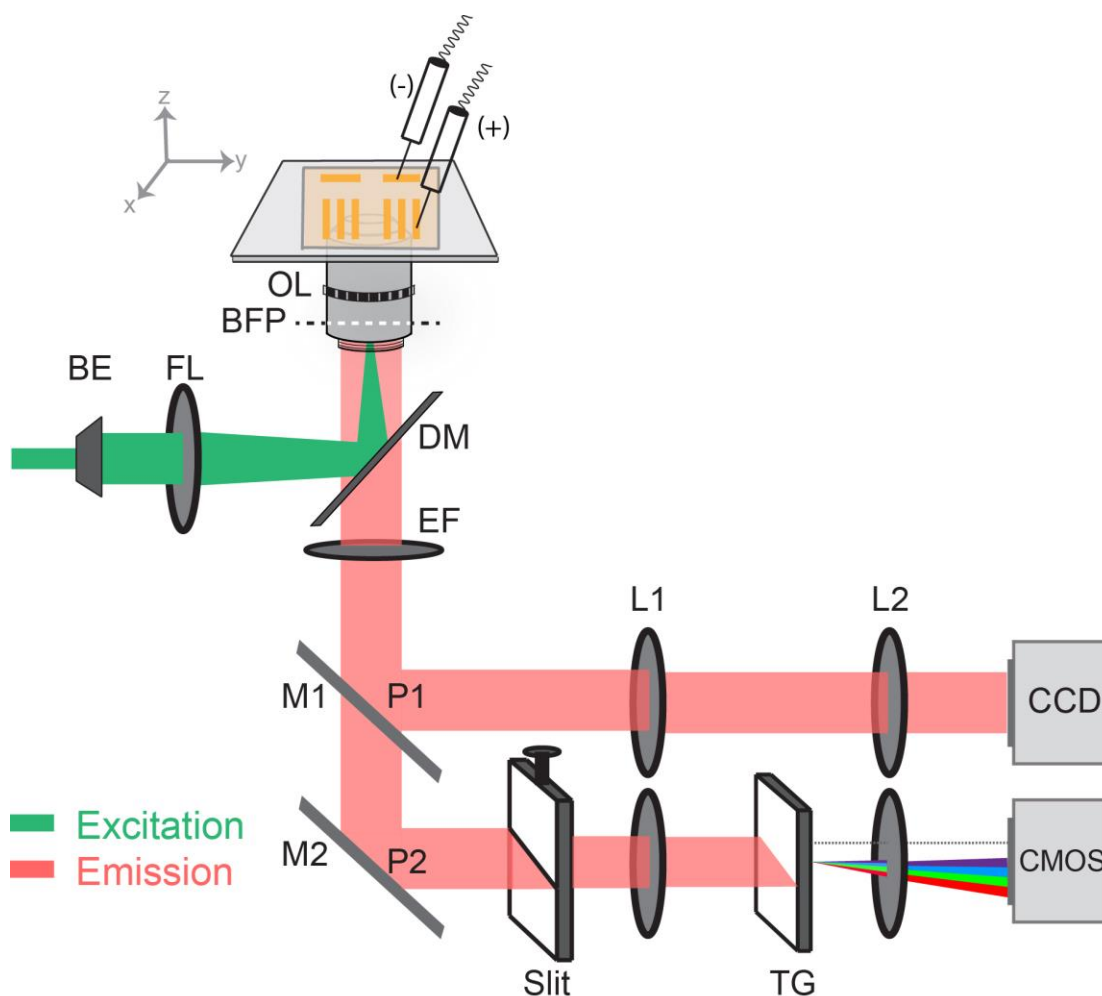
Characterization:

Current Voltage measurement (I-V measurement): *I-V* measurement was done by using an illuminator of Abet (Class A) Xenon lamp with KG-5 Filter, and using micromanipulator with

gold-coated probe (Holmarc). The light intensity was calibrated using silicon reference cells (Newport). An aperture of 0.03 cm^2 was used to describe the active area and SP-150 potentiostat was used as a source meter to measure the I-V characteristics.

Electrochemical impedance spectroscopy (EIS): EIS was performed using Autolab PGSTAT302N potentiostat in the range of 1 MHz to 0.01 Hz with 10 mV AC perturbation and spectra are collected with NOVA 2.5 software and analyzed with Z-view software.

Schematic S1. Schematic illustration of spatially resolved photo(electro)-luminescence micro-spectroscopy setup. (Abbreviations: BE-Beam expander; FL- Focusing Lens; BFP-Back Focal Plane; OL-Objective Lens; DM-Dichroic Mirror; EF-Emission Filter; P1, P2-emission paths; M1, M2-Highly reflective mirrors; L1, L2- tube lens; TG- Transmission Grating)

For spatially resolved photoluminescence (PL) and electroluminescence (EL) micro-spectroscopy measurements on solar cells/ devices, we used a home-built wide-field inverted epifluorescence microscope (Nikon Eclipse Ti2), the details of optical alignments are reported somewhere else. [3] For PL measurements, a continuous wave (CW) 532 nm DPSS laser (LRS-0532, Laserglow Tech.) circular excitation beam was focused at the back-focal plane (BFP) of an air objective lens (60X, 0.7 NA, S Plan Fluor, Nikon). This results in a wide circular excitation area (diameter~ 30 μm^2) in the sample plane. The excitation power was measured with a power meter (Coherent, lasercheck) after the objective lens and kept at ~ 1 $mWcm^{-2}$ for all the PL measurements. The fluorescence emission was collected back by the same objective lens and passed through the appropriate dichroic (z532rdc, Chroma Tech.) and emission filter (HQ665/250M, Chroma Tech.). For imaging, the emission was recorded with an air-cooled (−25 °C) interline CCD camera (DVC-1412AM) with an integration time of 500 milliseconds as 16-bit tiff files. For spectroscopy, an additional slit (Thorlabs, VA100/M) and 70 grooves/mm transmission grating (TG) were used in the emission path. The emission was recorded as spectral images with an air-cooled sCMOS camera (Hamamatsu, sCMOS ORCA-Flash4.0 V3) with an integration time of 2sec as 16-bit tiff files. The schematic setup for the PL-EL micro-spectroscopy measurements is shown in **Schematic S1**. For EL, the current was injected and controlled by a source meter (Keithley, 2450). The EL signal was detected in the same way as the PL signal. All the measurements were performed in the ambiance at room temperature (~ 295 K). The PL-EL imaging and spectroscopy data were analyzed using ImageJ (NIH). [4]

Electroluminescence Quantum yield measurement: To measure the quantum yield, the EL emission of the device was collected onto a calibrated Si-photodetector, which was placed in close proximity to the device. ELQY was calculated as:

$$ELQY = \frac{No.\,of\ photons\ emitted}{No.\,of\ charges\ injected} = \frac{P/hv}{I/e} \qquad \text{...(1)}$$

Where P is the output optical power, hv is the energy of the emitted photon, and I is the injected current.

XRD measurement: For phase confirmation and crystal structure, Rigaku Smartlab 9KW X-ray diffractometer (XRD) with source as Cu-Kα (1.54 Å) was used.

*SEM*: Field emission scanning electron microscope (FESEM) images were done using Carl-Zeiss Ultra 55 system.

TRPL: TRPL decay curves were collected with 10 s integration time, and a high-speed photomultiplier tube detector (Edinburgh) was used for the time-correlated single photon counting system. Monochromator width ($\Delta\lambda$) was fixed to 8 nm for all the measurements.

UV-VIS measurement: Optical absorption spectra were collected at room temperature using a PerkinElmer Lambda 1050+ spectrophotometer using an integrating sphere and $BaSO_4$ as a 100% reflectance reference. Low-temperature absorbance measurement was performed using the same spectrophotometer coupling it with an in-house closed-cycle helium cryostat.

MPPT measurement: The operational stability at MPPT is done either with Infinity PV LV-SMU (16 -MUX) assembled with active load or Keithley 2450 source meter under 1 sun continuous illumination in 60% relative humidity and at room temperature. Here, the voltage is applied and the corresponding power is tracked automatically. For the Vacuum experiment, we inserted our sample into a chamber assembled with a turbo and rotary pump, and the experiment is done with base pressure $5X10^{-5}$ torr.
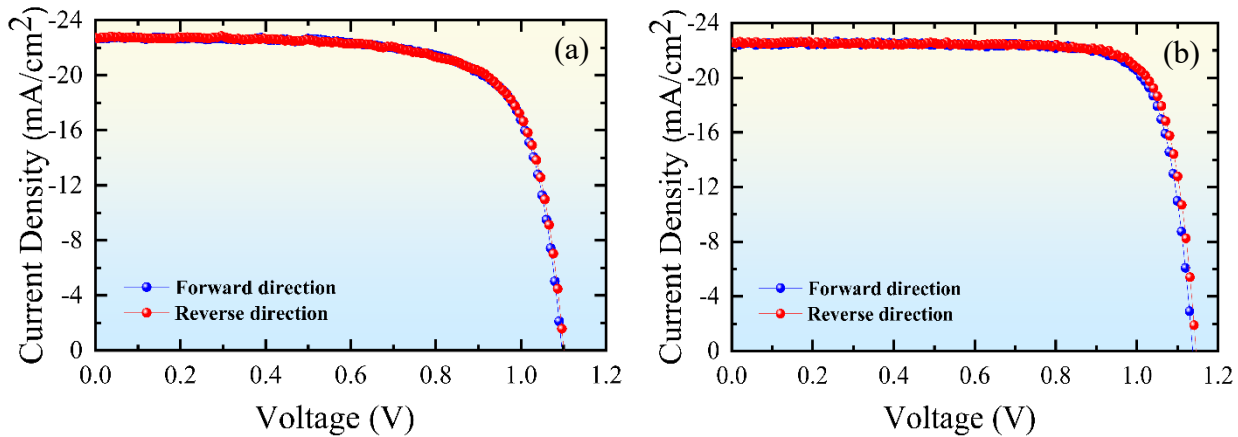
Figure S1. *J-V* characteristics of forward direction (Blue) and reverse direction (Red) of (a) Pristine (b) Coated devices showing negligible hysteresis.
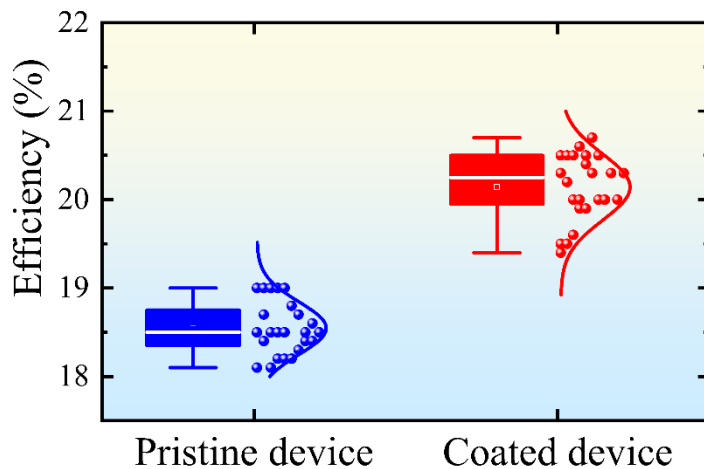

Figure S2. Statistical distribution of Efficiency for Pristine (Blue) and Coated device (Red).
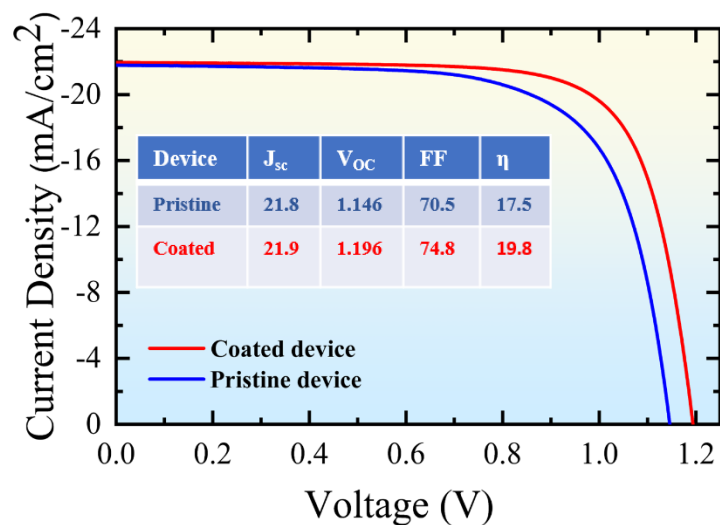
Figure S3. *J-V* characteristics of Pristine (Blue) and Coated device (Red) under full illumination.

We need to clarify here, that considering the reproducibility in measurements, all the devices results are measured with a shadow mask of an area of 0.03 cm^2 while the device active area is 0.12 cm^2. Thus, the recorded V_{OC}, reported here, is slightly lower than if otherwise measured under full device illumination, due to the persistent effect of the dark current contributed from the entire active area. [5] For one representative sample we found that the V_{OC} yields a value of 1.14 V for pristine and ~1.2 V for the coated one, as shown in Figure S3 under full device illumination. Furthermore, change of the ETL or the perovskite effectively substantiate the aforementioned observation
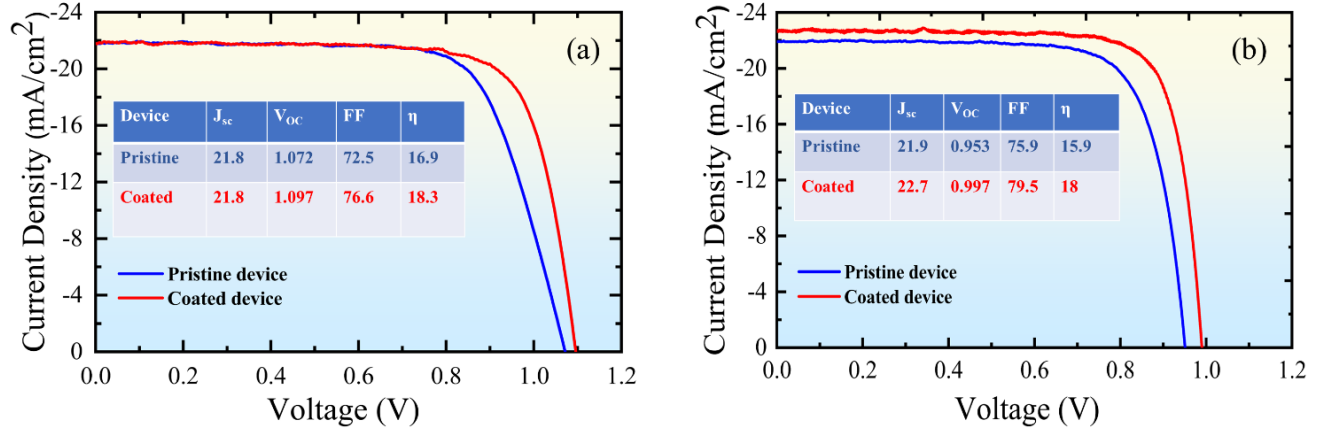
Figure S4. *J-V* characteristics Pristine (Blue) and Coated device (Red) (a) Planar TiO$_2$/MesoporousTiO$_2$/triple cation mixed halide perovskite/spiro-OMeTAD (b) SnO$_2$/MAPbI$_3$/spiro-OMeTAD based devices.

Here, a set of experiments are performed where the HTL and the ALD processes are kept invariant, but the underneath architecture is altered subsequently. With the same absorber layer, in the TiO2-based device the absolute change in the efficiency after the ALD coating is 1.4%, see Figure S4a, while the overall improvement is ~ 2.1% when the multi-cation perovskite is replaced with methylammonium lead iodide (MAPI), keeping SnO$_2$ as ETL, see Figure S4b. These results, even in unoptimized devices, suggest that the ETL-Perovskite interface has no major role to play in the enhancement of the overall device efficiency.
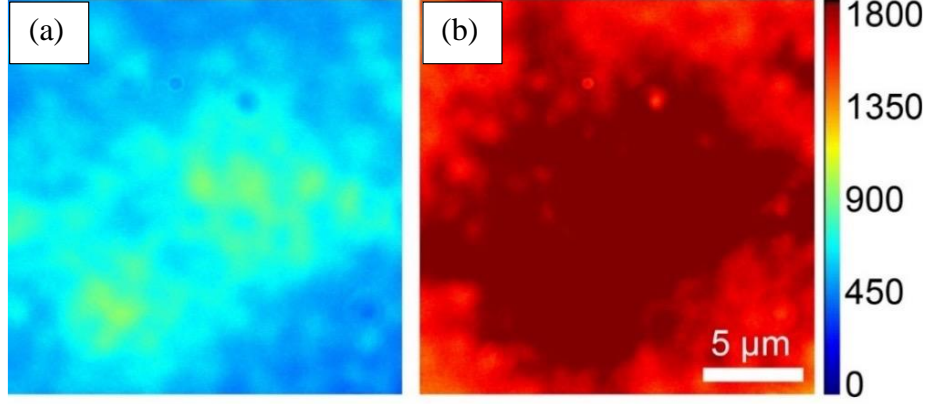
Figure S5. PL image of (a) Pristine and (b) Coated device where enhancement in PL is observed in Coated devices.

We have fitted the TRPL decay profile to a bi-exponential function given by

$$y = y_0 + a_1 e^{\left(-\frac{x}{t_1}\right)} + a_2 e^{\left(-\frac{x}{t_2}\right)} \qquad \ldots (2)$$

where y_0 is an offset, a_1 and a_2 are weight constants, and t_1 and t_2 are time decay constants.

The relative contributions of the two decay channels (I_1 and I_2) as a percentage of total PL intensity is given by the following equations:

$$I_1(\%) = \frac{a_1 t_1}{a_1 t_1 + a_2 t_2} \qquad \ldots (3)$$

$$I_2(\%) = \frac{a_2 t_2}{a_1 t_1 + a_2 t_2} \qquad \ldots (4)$$

The extracted bi-exponential fitting on the coated and pristine half-cell samples are shown in Figures S6 and S7 and the extracted parameters are tabulated in Table S1 and Table S2. From the fitting parameters, it is clear that for both the coated and pristine half-cell samples the lifetime of the dominant decay, the channel is dramatically different. In the case of pristine half-cell, the

14

lifetime of the dominant decay channel (contributing more than 90% of the total PL emission) is ~ 17 ns and essentially does not vary with the emission wavelength which is a key indicator of this channel to be a band-edge emission. On the other hand, we found a significant wavelength variation in the lifetime of the dominant decay channel for the pristine half-cell sample which is tabulated in Table S2. The lifetime of the dominant channel increases with the increase of emission wavelength indicating that the defect emission plays a major role towards the high wavelength side. In this case, it is clear that the dominant channel contains both the band-edge and defect emission and bi-exponential fitting is not sufficient to separate them.

In order to distinguish the bandgap and defect emission contributions in the pristine half-cell we have carried out a tri-exponential fitting for this sample. In this case, we assume that the band-edge emission properties do not change with the ALD coating and fixed the lifetime of the dominant channel of the coated half-cell as the band-edge emission. Then we took these values to fit the pristine half-cell sample with tri-exponential function. We freely vary the parameters associated with the first and third components whereas fixing the lifetimes of the second components as the lifetimes of the band-edge emissions. The triexponential fitting function is given below,

$$ y = y_0 + a_1 e^{\left(-\frac{x}{t_1}\right)} + a_2 e^{\left(-\frac{x}{t_2}\right)} + a_3 e^{\left(-\frac{x}{t_3}\right)} \qquad \qquad \dots (5) $$

where y_0 is an offset, a_1, a_2 and a_3 are weight constants, and t_1, t_2 and t_3 are time decay constants.

The relative contributions of the three decay channels (I_1, I_2 and I_3) as a percentage of total PL intensity is given by the following equations:

$$I_1(\%) = \frac{a_1 t_1}{a_1 t_1 + a_2 t_2 + a_3 t_3} \qquad \qquad \ldots (6)$$

$$I_2(\%) = \frac{a_2 t_2}{a_1 t_1 + a_2 t_2 + a_3 t_3} \qquad \qquad \ldots (7)$$

$$I_3(\%) = \frac{a_3 t_3}{a_1 t_1 + a_2 t_2 + a_3 t_3} \qquad \qquad \ldots (8)$$

In this fitting, we observed very fast (~ 3 ns) and the least contributing (less than 5 %) first channel which is similar to that of the faster component of coated samples in the bi-exponential fitting. The second component is essentially due to the band-edge emission which we fixed and the third component is due to the long-lived dominant defect emission. The fitting is shown in Figure S8 and the extracted parameters are tabulated in Table S3.
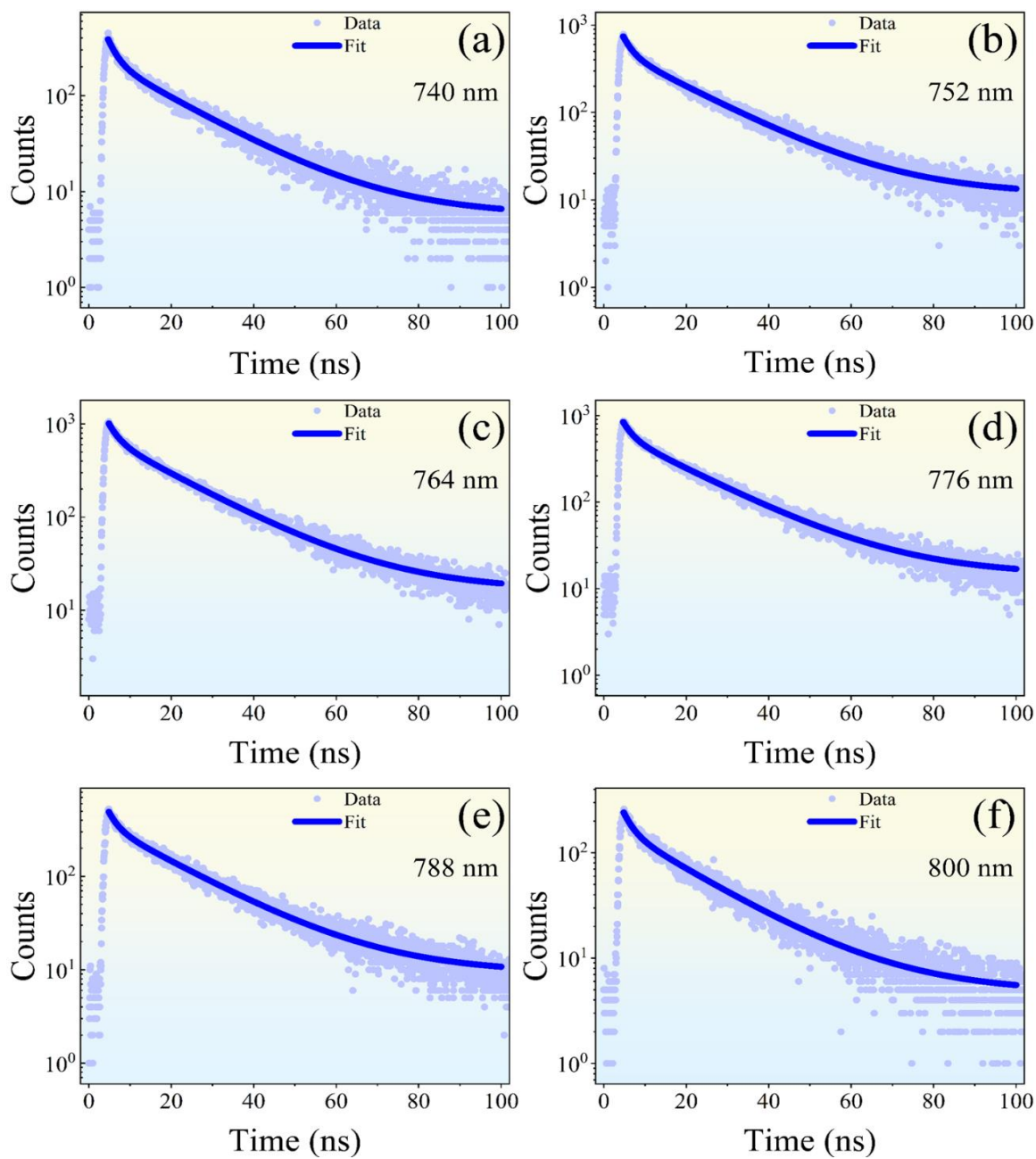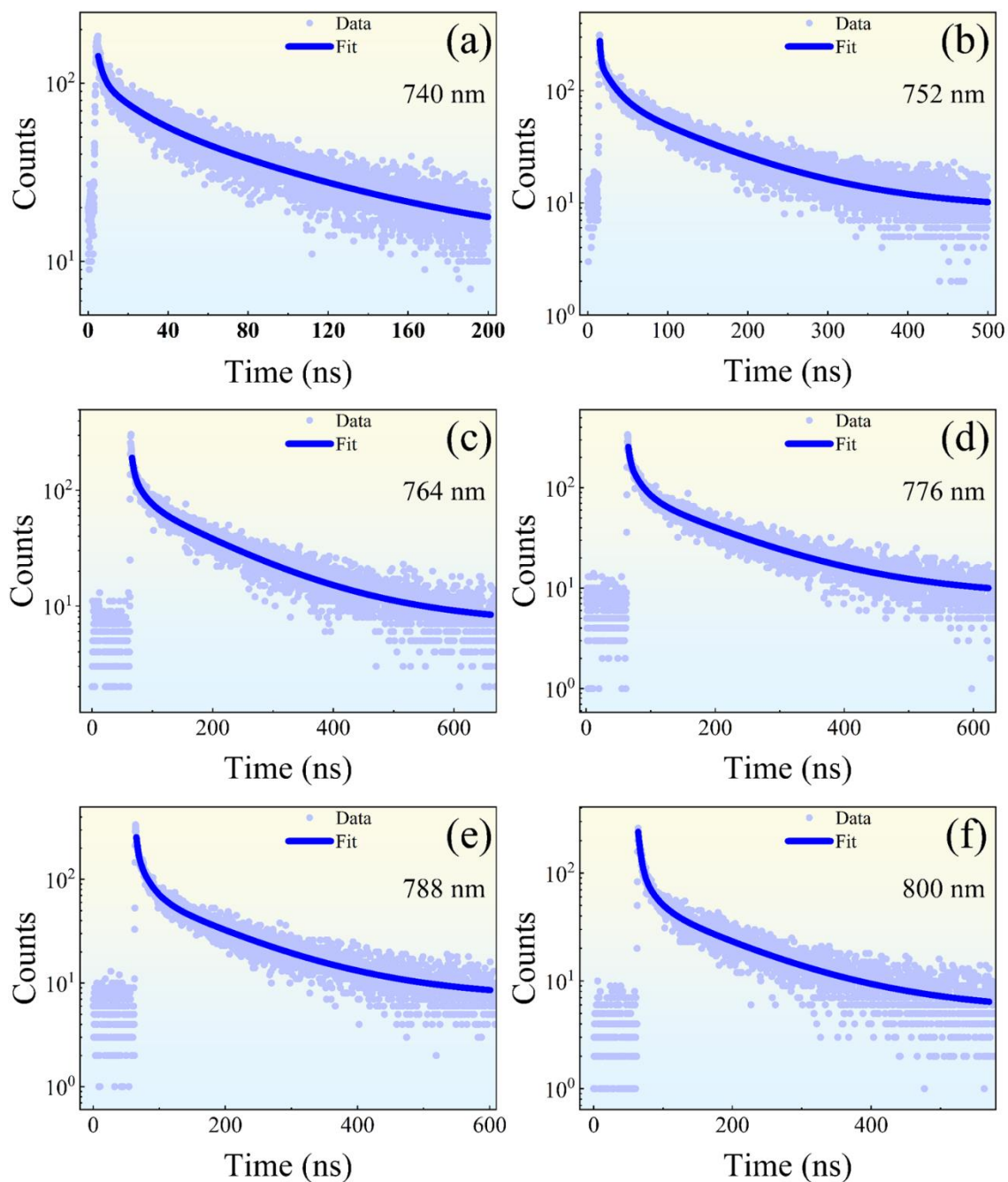
Figure S6. Time-resolved photoluminescence spectra collected on coated half-cell at different emission wavelengths – (a) 740 nm, (b) 752 nm, (c) 764 nm, (d) 776 nm, (e) 788 nm, and (f) 800 nm. The solid lines indicate the bi-exponential fitting of the experimental data.
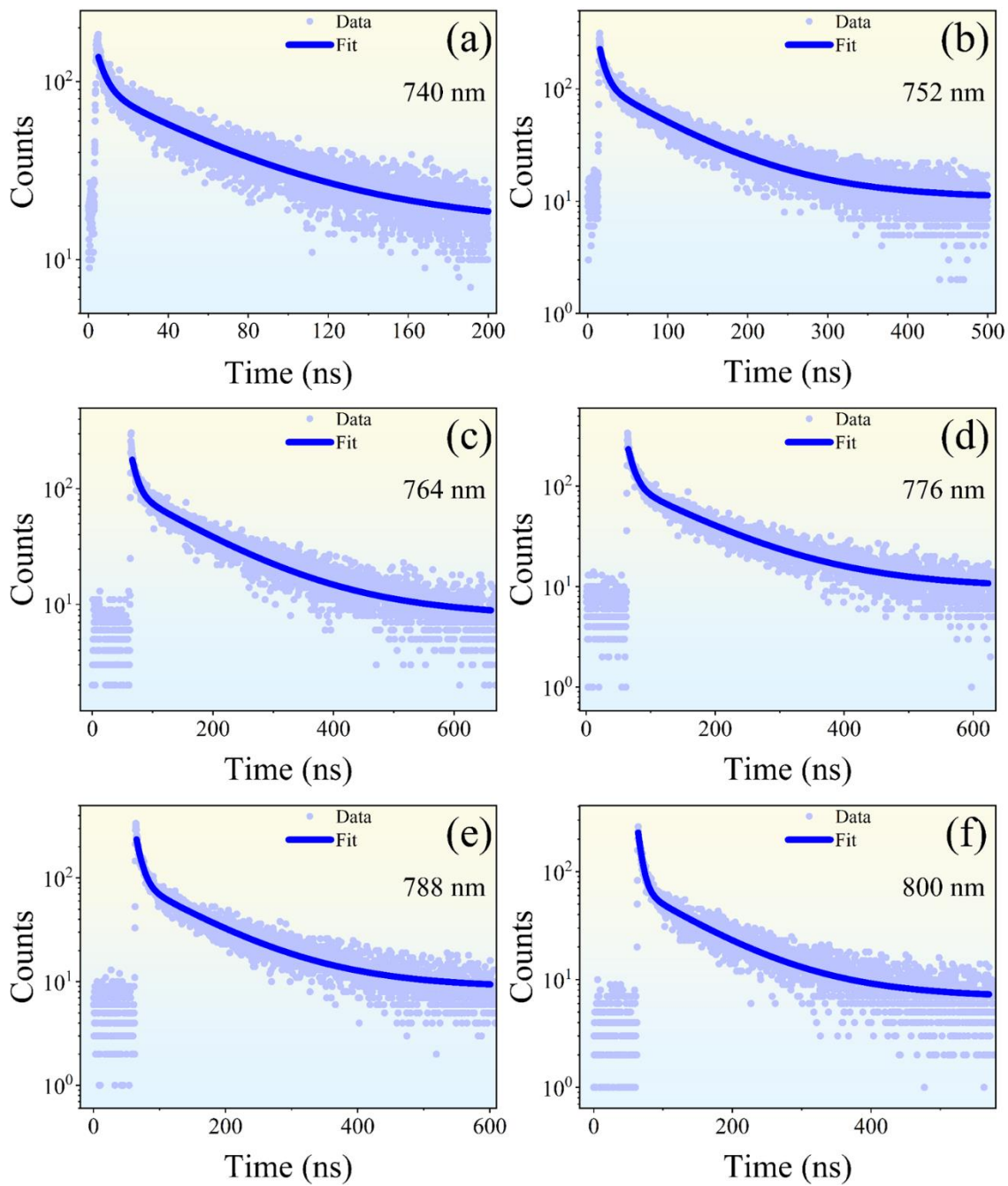
Figure S7. Time-resolved photoluminescence spectra collected on pristine half-cell at different emission wavelengths (a) 740 nm, (b) 752 nm, (c) 764 nm, (d) 776 nm, (e) 788 nm, and (f) 800 nm. The solid lines indicate the bi-exponential fitting of the experimental data.

Figure S8. Time resolved photoluminescence spectra collected on pristine half-cell at different emission wavelengths (a) 740 nm, (b) 752 nm, (c) 764 nm, (d) 776 nm, (e) 788 nm and (f) 800 nm. The solid lines indicate the tri-exponential fitting of the experimental data.

Table S1: The extracted parameters from the bi-exponential fitting of the TRPL data collected on the coated half-cell:

Emission wavelength (nm)	A_1	A_2	t_1 (ns)	t_2 (ns)
727	71.99 ± 2.39	115.13 ± 1.82	2.07 ± 0.13 **(7.95%)**	16.48 ± 0.58 **(92.05%)**
740	165.01 ± 2.74	217.09 ± 2.31	2.25 ± 0.07 **(8.88%)**	17.58 ± 0.23 **(91.12%)**
752	276.10 ± 3.86	453.08 ± 3.21	2.20 ± 0.06 **(7.13%)**	17.46 ± 0.15 **(92.87%)**
764	343.90 ± 4.83	654.04 ± 4.15	2.34 ± 0.06 **(6.47%)**	17.79 ± 0.14 **(93.52%)**
776	275.48 ± 4.27	550.02 ± 3.57	2.25 ± 0.07 **(5.98%)**	17.73 ± 0.14 **(94.02%)**
788	161.78 ± 3.33	322.29 ± 2.69	2.16 ± 0.09 **(5.76%)**	17.76 ± 0.19 **(94.24%)**
800	84.13 ± 2.21	153.05 ± 1.85	2.32 ± 0.12 **(6.56%)**	18.14 ± 0.27 **(93.44%)**

Table S2: The extracted parameters from the bi-exponential fitting of the TRPL data collected on the pristine half-cell:

| Emission wavelength (nm)	A_1	A_2	t_1 (ns)	t_2 (ns)
727	21.78 ± 1.21	43.37 ± 0.52	2.29 ± 0.25 **(3.18%)**	35.04 ± 1.57 **(96.82%)**
740	48.44 ± 1.38	73.69 ± 0.67	4.53 ± 0.26 **(4.55%)**	62.49 ± 1.49 **(95.45%)**
752	117.78 ± 1.59	98.57 ± 0.86	7.63 ± 0.20 **(8.72%)**	95.45 ± 1.28 **(91.28%)**
764	79.45 ± 1.52	81.98 ± 0.83	9.44 ± 0.36 **(6.38%)**	134.34 ± 2.45 **(93.62%)**
776	133.47 ± 1.94	90.43 ± 1.02	9.74 ± 0.28 **(10.27%)**	125.62 ± 2.47 **(89.73%)**
788	148.21 ± 1.81	79.93 ± 0.94	8.60 ± 0.20 **(12.52%)**	112.87 ± 2.22 **(87.48%)**
800	162.46 ± 1.87	60.38 ± 0.79	6.35 ± 0.14 **(14.13%)**	103.89 ± 2.34 **(85.87%)**

Table S3: The extracted parameters from the tri-exponential fitting of the TRPL data collected on the pristine half-cell:

Emission wavelength (nm)	A_1		A_2		A_3		t_1 (ns)		t_2 (ns)		t_3 (ns)	
740	37.48 ± 3.28		32.35 ± 4.44		61.29 ± 4.57		2.50 ± 0.37 (1.53%)		17.58 ± 4.32 (9.35%)		88.47 ± 12.75 (89.11%)	
752	100.34 ± 3.42		88.08 ± 1.84		80.75 ± 1.52		1.25 ± 0.08 (1.10%)		17.46 ± 0.74 (13.56%)		119.89 ± 3.01 (85.34%)	
764	38.05 ± 5.99		53.92 ± 4.94		75.68 ± 1.53		3.29 ± 0.59 (1.01%)		17.79 ± 2.11 (7.74%)		149.37 ± 4.41 (91.25%)	
776	74.79 ± 5.59		92.97 ± 4.83		79.99 ± 1.72		2.81 ± 0.36 (1.54%)		17.73 ± 1.29 (12.08%)		147.29 ± 4.84 (86.38%)	
788	92.08 ± 6.05		89.73 ± 5.45		66.35 ± 1.73		3.34 ± 0.33 (2.75%)		17.76 ± 1.38 (14.26%)		139.84 ± 5.24 (82.99%)	
800	127.84 ± 7.12		59.42 ± 6.50		48.54 ± 1.82		3.96 ± 0.28 (6.14%)		18.14 ± 2.31 (13.07%)		137.26 ± 7.33 (80.79%)	
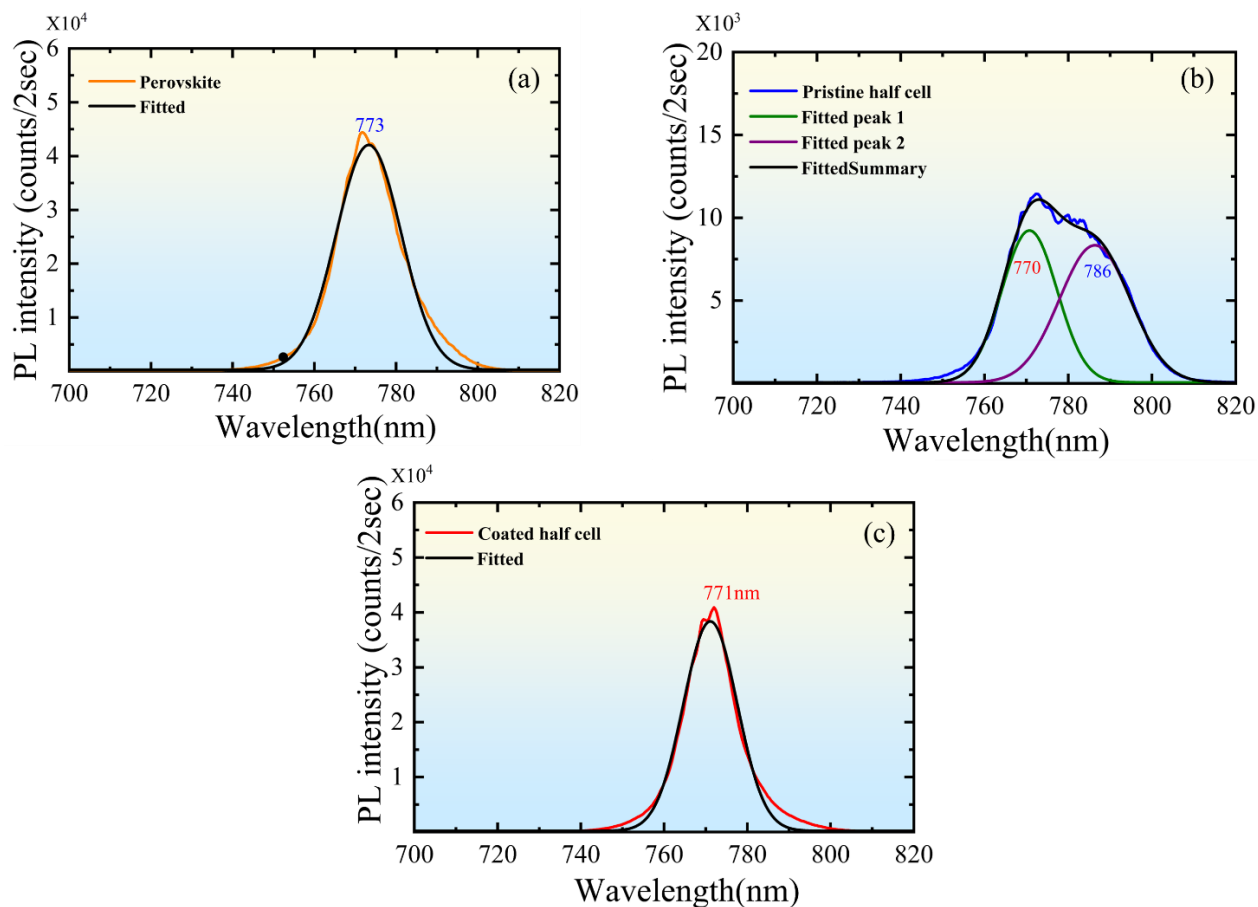
Figure S9. Deconvolution of PL peaks at 100K are depicted (a) Perovskite film in orange color (PL peak at 773nm) (b) Pristine half-cell in blue color (PL peak at 770nm and &786nm) (c) Coated half -cell in red color (PL peak at 771nm).

One obvious change between the room-temperature (Figure 2a) and the low-temperature emission spectra (See Figure S9) is the blue-shift of 20 nm that is essentially due to the lattice contraction .
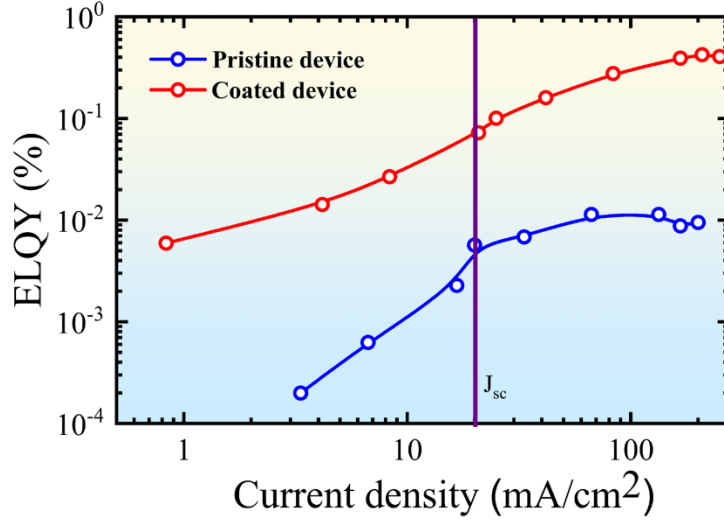
Figure S10. Variation in ELQY with injection current density measured on Pristine and Coated devices.

Notably, in our case, a small but consistent blue shift (6 nm) is noted in the coated sample which is in concurrence with the previously reported observations [6] where such trends were used to suggest a lowered density of sub-bandgap states that mediate the non-radiative recombination. Following our previous discussion, the EL intensity (Inset of Figure 3b) is also significantly higher for the coated device compared to the pristine device so the EL quantum yield (ELQY) which is enhanced by an order of magnitude (Figure 3b), once again proving the effective ALD-induced removal of the non-radiative defect centers that are responsible for reducing the V_{OC} loss due to the nonradiative recombination, ΔV_{nr}, and pushing towards its radiative limit. This reduction of the voltage (ΔV_{nr}) can be quantitatively estimated by the reciprocity theorem [7] and mathematically expressed as

$$\Delta V_{nr} = -kT \, ln(ELQY) \qquad -- \qquad (9)$$

The above equation explicitly articulates the fact that higher ELQY corresponds to lowered non-radiative losses. The average measured ELQY and the estimated ΔV_{nr} values of representative pristine and coated samples are presented in Table S4. The coated devices are characterized by a reduced $\Delta V_{nr} \approx 176\ mV$. Furthermore, from the obtained ELQY values, the estimated difference in the voltage losses between the pristine and coated samples is ~62$\pm$7 mV which is in close agreement with the measured V_{OC} improvement (64 mV) in these devices, before and after the ALD coating. Furthermore, Figure S10 shows the ELQY for injection currents that was varied by approximately three orders of magnitude. The coated devices show EL switch-on characteristics even at relatively smaller currents in comparison to the pristine devices. Moreover, the ELQY is consistently higher by an order of magnitude across the range of the applied current densities. At higher current density (> 100 mA/cm^2), the efficiency roll-off is significantly reduced in the treated devices. The ELQY is ~0.4 % at an applied current density of 100 mA.cm^{-2}, which is comparable to previous observations in high-performance solar cell devices. [8-9] Thus, the EL measurements and subsequent analysis, confirm that the ALD coating on the perovskite solar cells majorly suppresses the non-radiative pathways leading to considerably higher device performances.

Table S4: Percentage of EL quantum yield (ELQY) collected from Pristine and Coated devices and corresponding ΔVnr of Pristine and Coated device calculated using equation 1. From that ΔV (V_{oc} difference in both devices) is calculated which is close to the experimental result.

Device	ELQY (%)	$-\Delta V_{nr}$ (mV)	V_{oc} (V)
Pristine	0.0073 ± 0.0046	238 ± 18	1.078
Coated	0.08725 ± 0.023	176 ± 7	1.142
ΔV		62 ± 7	64 mV
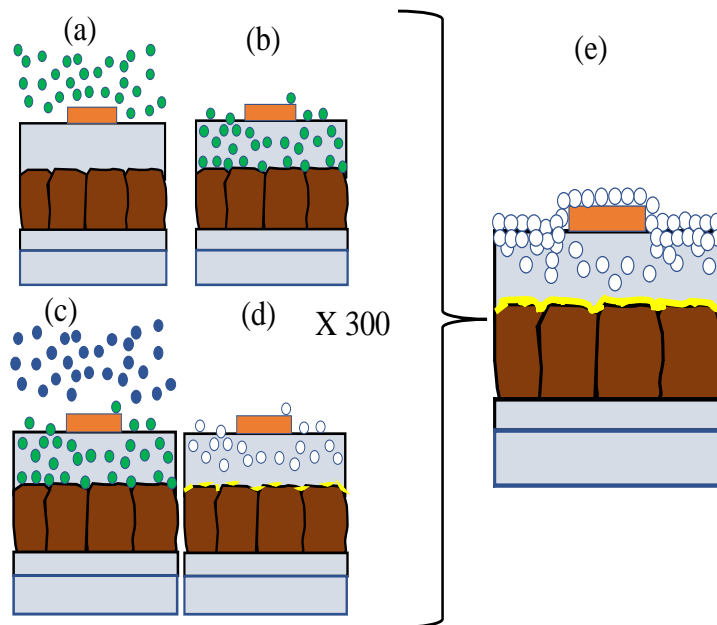
Figure S11. Schematic representation of ALD process is shown where (a) and (b) represent infiltration of TMA (Green circle) inside spiro in the first half cycle. (c) The next half cycle demonstrates H_2O molecule's (Blue) reaction mechanism on the device. (d) Representation of formation of Al_2O_3 (white circle) on devices after 300 cycles resulting in PbI_2 formation as depicted in (e).

We have previously shown that the TMA infiltrates into the spiro layer. This is based on the in-situ QCM analysis where the mass consecutively increases with successive TMA dosages but levels off eventually. During the first dose of TMA, it is hence get infiltrated and physisorbed inside the spiro layer as schematically shown in Figure S11a. During the second half-cycle of the ALD process, when water vapor is dosed into the reactor, it reacts only to the near-surface TMA species as the H_2O molecule does not soak into the spiro layer. This process results in the Al_2O_3 nucleation at or near the surface region only and leaves behind some unreacted TMA molecule in the bulk of the spiro, as shown schematically in Figure S11b. Considering the fact that the nucleated Al_2O_3 provides favorable reaction site during the second cycle so understandably the

fraction of the TMA gets consumed and fractional reduction of the unreacted soaked TMA inside the spiro layer can be hypothesized. Furthermore, the process gets proportionally higher in consecutive cycles to a limit till the surface is covered with Al_2O_3, see Figure S11c, and embarks to the linear growth regime.

As mentioned in the manuscript that the set of the TMA molecules that do not contribute to the reaction to form Al_2O_3 can react to the perovskite surface to form PbI_2 and with the consecutive cycles, and only during the nucleation regime of the Al_2O_3, the formation of PbI_2 get proportional and hence the dosage (Langmuir) of the TMA and H_2O is important so as the purge time, which is the time between two consecutive ALD half-cycles. To reduce the dwelling time of the device at elevated temperature and under vacuum, the purging time is generally reduced to an extent where chemical vapor deposition (CVD) can be avoided. The purging time, in turn, depends on the pumping efficiency, which depends on the architecture of the ALD reactor. For the reactor involved in this work, we found that the 10 sec purging is the minimum to drive the ALD reaction. However, it is important to keep in mind that the physisorption TMA is likely to be reversible due to the process condition, high temperature (70 ^{o}C), and low vacuum (~ 1 Torr). Hence it is likely that with higher purging time, TMA desorbs out. This is well understood from the fact that with 30 sec purging time, little V_{OC} improvement is noticed as shown in Figure S14.

It is to be noted that the optimized device performance, we have applied 300 cycle of ALD Al_2O_3 on top of the fully functional device (including Au contact) as shown schematically in the figure S11. Under the ideal scenario (on hydroxy terminated Si-SiO_2 surface, each ALD cycle with the dose conditions, mentioned above, leads to average thickness of 0.12nm, hence ideally the thickness is likely to be 36nm. But due to, the non-linear nucleation of the Al_2O_3 on spiro surely leads to certain deviation from the standard calculation.

The samples were taken out of the ALD reactor soon after the reaction get completed.

Understandably enough, only TMA dosages can also serve the purpose but in that case, the Al_2O_3 encapsulation is unlikely to happen and the device stability gets compromised. Nevertheless, the thermal treatment during the course of the ALD process (70 °C) cannot be always ignored as the perovskite material by itself is sensitive to temperature. Our observations, however, reveal no significant behavioral changes in the device performances, before and after the specified thermal conditioning, and hence, ignored.
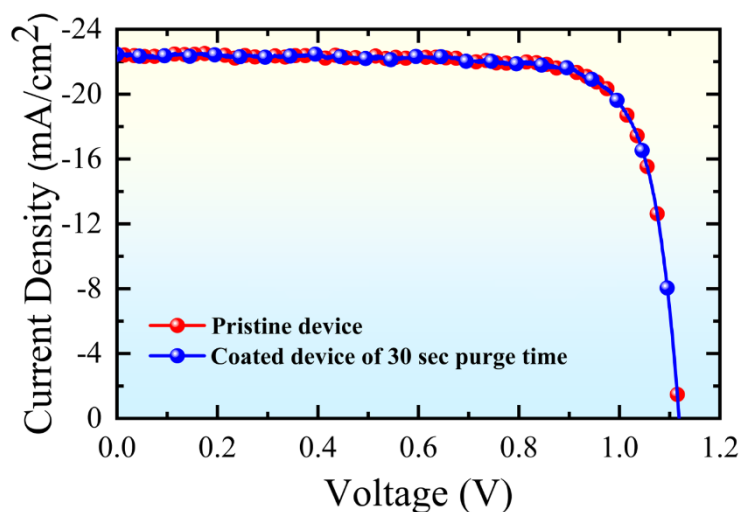

Figure S12. *J-V* characteristics of effect of long purging time (30 sec) of Pristine (Blue) and Coated (Red) device showing negligible improvement /change in device performance.

While looking from the ALD point of view, the higher purging time between the consecutive dosages of chemicals allows the infiltrated TMA to diffuse out of the spiro layer due to the reversibility of the physisorption process. Under such deposition conditions, the V_{OC} improvement is negligible as shown in Figure S12. Considering these, we believe that there is further room for

optimization that may lead to additional improvement; however, such optimization is beyond the

scope and the aim of the present work.
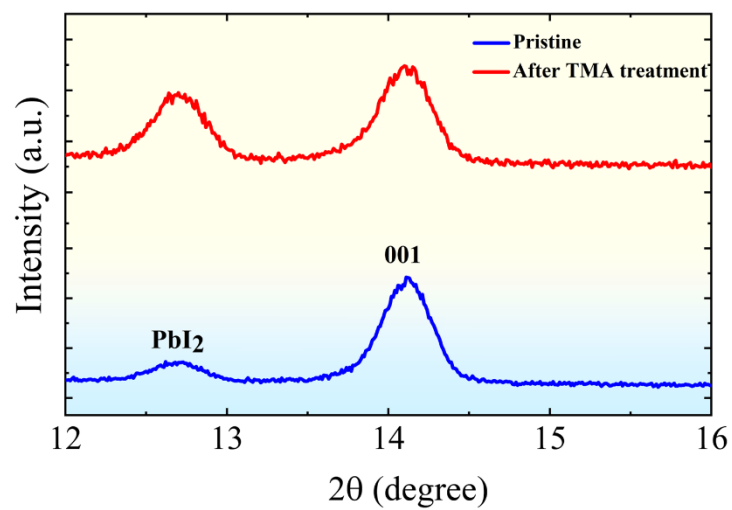
Figure S13. XRD of Pristine (Blue) and after TMA treatment (Red) depicting presence of prominent

PbI_2 peak (12.7^0) after TMA treatment.
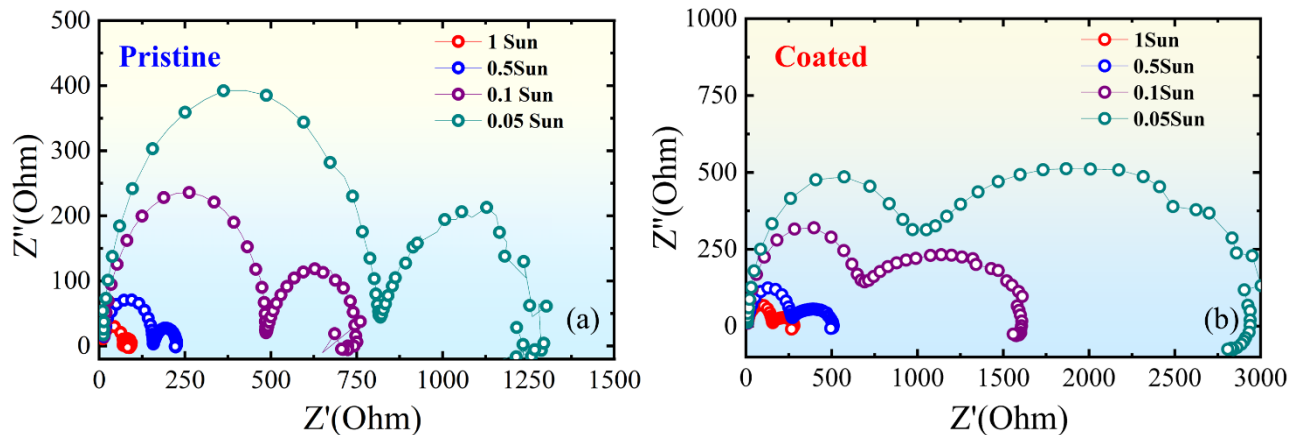
Figure S14. Nyquist plots under different illumination intensity 1 sun (Red),0.5 Sun (Blue), 0.1 Sun (Purple),0.05 Sun (Cyan Blue)) in the case of (a) Pristine (b) Coated devices at V_{OC} condition.
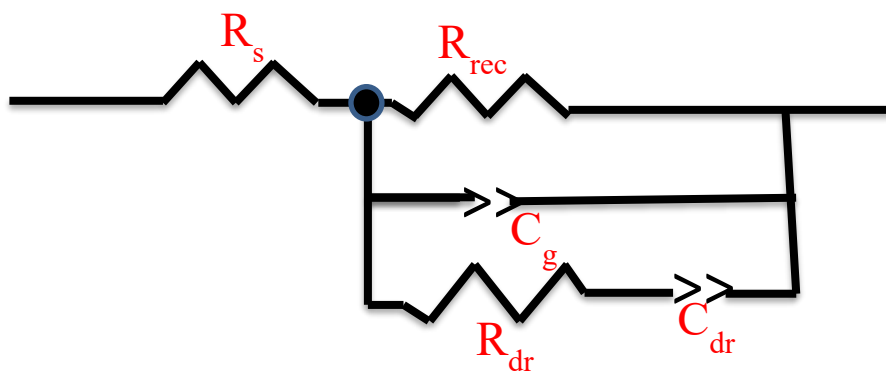
Figure S15. Circuit that is used in the fitting of impedance analysis where R_s representing series resistance and R_{rec} representing resistance that are coming from combined contribution of recombination and charge transport resistance, R_{dr} dr like-low frequency resistance branch and C_{dr} dr- like low frequency capacitance.
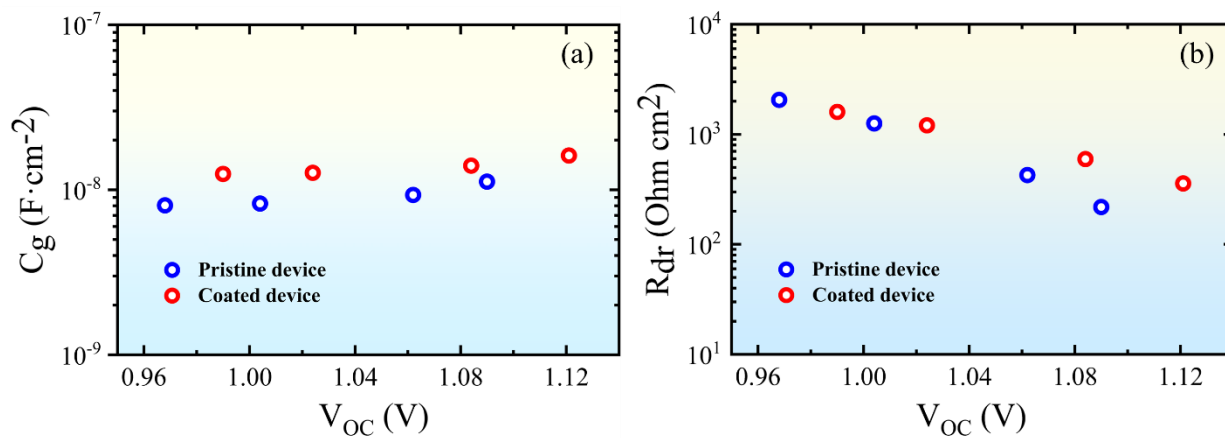
Figure S16. (a) Geometrical capacitance of Pristine (Blue) and Coated (Red) device depicting no change in geometrical capacitance (b) Low frequency branch R_{dr} of Pristine (Blue) and Coated (Red) device depicting slight increase particularly shown at high charge carrier concentration in Coated device.

REFERENCES

1.   Groner, M. D.; Fabreguette, F. H.; Elam, J. W.; George, S. M., Low-Temperature Al2O3 Atomic Layer Deposition. *Chemistry of Materials* **2004,** *16* (4), 639-645. https://doi.org/10.1021/cm0304546

2.   Mahuli, N.; Sarkar, S. K., Atomic layer deposition of NiS and its application as cathode material in dye sensitized solar cell. *Journal of Vacuum Science & Technology A* **2016,** *34* (1), 01A142. https://doi.org/10.1116/1.4938078.

3.   De, S.; Layek, A.; Raja, A.; Kadir, A.; Gokhale, M. R.; Bhattacharya, A.; Dhar, S.; Chowdhury, A., Two Distinct Origins of Highly Localized Luminescent Centers within InGaN/GaN Quantum-Well Light-Emitting Diodes. *Advanced Functional Materials* **2011,** *21* (20), 3828-3835. https://doi.org/10.1002/adfm.201100894.

4.   Schneider, C. A.; Rasband, W. S.; Eliceiri, K. W., NIH Image to ImageJ: 25 years of image analysis. *Nature Methods* **2012,** *9* (7), 671-675. https://doi.org/10.1038/nmeth.2089

5. Kiermasch, D.; Gil-Escrig, L.; Bolink, H. J.; Tvingstedt, K. Effects of Masking on Open-Circuit Voltage and Fill Factor in Solar Cells. *Joule* **2019**, *3* (1), 16-26. DOI: https://doi.org/10.1016/j.joule.2018.10.016.

6. Yu, H.; Wang, H.; Zhang, T.; Yi, C.; Zheng, G.; Yin, C.; Karlsson, M.; Qin, J.; Wang, J.; Liu, X.-K.; et al. Color-Stable Blue Light-Emitting Diodes Enabled by Effective Passivation of Mixed Halide Perovskites. The Journal of Physical Chemistry Letters 2021, 12 (26), 6041-6047. DOI: 10.1021/acs.jpclett.1c01547.

7. Rau, U. Reciprocity relation between photovoltaic quantum efficiency and electroluminescent emission of solar cells. Physical Review B 2007, 76 (8), 085303. DOI: 10.1103/PhysRevB.76.085303.

8. Rai, M.; Wong, L. H.; Etgar, L. Effect of Perovskite Thickness on Electroluminescence and Solar Cell Conversion Efficiency. The Journal of Physical Chemistry Letters 2020, 11 (19), 8189-8194. DOI: 10.1021/acs.jpclett.0c02363. Bi, D.; Tress, W.; Dar, M. I.; Gao, P.; Luo, J.; Renevier, C.; Schenk, K.; Abate, A.; Giordano, F.; Correa Baena, J.-P.; et al. Efficient luminescent solar cells based on tailored mixed-cation perovskites. Science Advances 2016, 2 (1), e1501170. DOI: doi:10.1126/sciadv.1501170.

9. Singh, R.; Ghosh, S.; Subbiah, A. S.; Mahuli, N.; Sarkar, S. K. ALD Al2O3 on hybrid perovskite solar cells: Unveiling the growth mechanism and long-term stability. Solar Energy Materials and Solar Cells 2020, 205, 110289. DOI: https://doi.org/10.1016/j.solmat.2019.110289.